

# Deuteration of $\text{HC}_3\text{N}$ and $\text{CH}_3\text{CCH}$ in the pre-stellar core L1544

K. Giers<sup>1</sup>, S. Spezzano<sup>1</sup>, Y. Lin<sup>1</sup>, P. Caselli<sup>1</sup>, O. Sipilä<sup>1</sup>

Max-Planck-Institute for Extraterrestrial Physics, Giessenbachstrasse 1, D-85748 Garching, Germany  
e-mail: kgiers@mpe.mpg.de

January 23, 2026

## ABSTRACT

**Context.** Deuterated molecules are a useful diagnostic tool to probe the evolution and the kinematics in the earliest stages of star formation. Due to the low temperatures and high densities in the centre of pre-stellar cores, the deuterium fraction is enhanced by several orders of magnitude with respect to the cosmic D/H abundance ratio.

**Aims.** We study the distribution of the emission and the deuteration of the two carbon chains  $\text{HC}_3\text{N}$  and  $\text{CH}_3\text{CCH}$  throughout the prototypical pre-stellar core L1544.

**Methods.** We analyse emission maps of  $\text{CH}_3\text{CCH}$ ,  $\text{CH}_2\text{DCCH}$ ,  $\text{CH}_3\text{CCD}$ ,  $\text{HC}_3\text{N}$ ,  $\text{HCC}^{13}\text{CN}$ , and  $\text{DC}_3\text{N}$ , observed towards L1544 with the IRAM 30 m single-dish radio telescope. We use non-local thermodynamic equilibrium radiative transfer calculations, combined with chemical modelling of the molecular abundances, to constrain physical parameters of the observed species. Following this, we derive the corresponding column density and deuteration maps and analyse the chemical processes influencing the different molecular distributions.

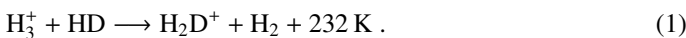
**Results.** We find levels of deuteration of  $\text{N}(\text{DC}_3\text{N})/\text{N}(\text{HC}_3\text{N}) = 0.04 - 0.07$ ,  $\text{N}(\text{CH}_2\text{DCCH})/\text{N}(\text{CH}_3\text{CCH}) = 0.09 - 0.15$ , and  $\text{N}(\text{CH}_3\text{CCD})/\text{N}(\text{CH}_3\text{CCH}) = 0.07 - 0.09$ . The deuteration of  $\text{HC}_3\text{N}$  appears homogeneous across the core, with widespread D-fraction values above 0.06, tracing intermediate-density gas in the outer layers of the core, at densities less than  $10^5 \text{ cm}^{-3}$ .  $\text{CH}_3\text{CCD}$  is most efficiently formed in the higher-density regions towards the core centre, while the deuteration fraction of  $\text{CH}_2\text{DCCH}$  traces a local density enhancement in the north-east of the core, coinciding with the  $\text{CH}_3\text{OH}$  emission peak.

**Conclusions.** The results suggest that gas-phase reactions dominate the formation and deuteration of both  $\text{HC}_3\text{N}$  and  $\text{CH}_3\text{CCH}$  in L1544, with spatial variations driven by physical structure, density and external radiation. The significantly higher deuteration fraction of  $\text{CH}_2\text{DCCH}$  compared to  $\text{CH}_3\text{CCD}$  and a tentative gradient with higher values in the north suggest that there are different deuteration mechanisms for the two functional groups, with varying efficiency across the core. Similarities between the  $\text{CH}_2\text{DCCH}$  emission and  $\text{CH}_2\text{DOH}$  might indicate an additional deuteration pathway of  $\text{CH}_3\text{CCH}$  on the surfaces of dust grains, as observed for  $\text{H}_2\text{CO}$ .

**Key words.** astrochemistry – ISM: clouds – ISM: molecules – ISM: abundances – stars: formation

## 1. Introduction

Deuterium fractionation of molecules is a powerful tool to study the early stages of star formation. Due to the combination of high densities and low temperatures in the pre-stellar phase, CO is largely depleted onto the surfaces of dust grains (see e.g. Caselli et al. 1999). As CO is the main destroyer of several ions (e.g.  $\text{H}_3^+$  and its deuterated forms; Dalgarno & Lepp 1984), its depletion leads to an enhancement in their abundances. Simultaneously, the main pathway for the formation of  $\text{H}_2\text{D}^+$  opens up:



As this reaction is exothermic, the backwards reaction is suppressed at the low temperatures present in pre-stellar cores (assuming a low ortho-to-para  $\text{H}_2$  ratio; e.g. Pagani et al. 1992). The enhanced abundance of  $\text{H}_2\text{D}^+$ , as well as of  $\text{D}_2\text{H}^+$  and  $\text{D}_3^+$ , then leads to an increased deuteration of other molecules, via a deuteron transfer, as predicted by models (e.g. Walmsley et al. 2004).

The evolved pre-stellar core L1544 is known for its high levels of deuteration (see e.g. Crapsi et al. 2005; Chantzos et al. 2018; Giers et al. 2023). The distribution of the deuterium fractionation across this core has been studied for a variety of molecules:  $\text{HCO}^+$ ,  $\text{N}_2\text{H}^+$ ,  $\text{CH}_3\text{OH}$ ,  $\text{H}_2\text{CO}$ ,  $\text{c-C}_3\text{H}_2$ , and  $\text{H}_2\text{CS}$  (Caselli et al. 2002a; Redaelli et al. 2019; Chacón-Tanarro et al.

2019; Giers et al. 2022; Spezzano et al. 2022). Those observations show that, for most species, the deuterium fractionation in L1544 is most efficient in the central regions of the core, indicated by the dust continuum peak, in higher-density gas layers. On the other hand, the different molecules show a wide range of deuteration levels: while  $\text{H}_2\text{CO}$  and  $\text{HCO}^+$  show rather low values of around 3%,  $\text{N}_2\text{H}^+$  and  $\text{H}_2\text{CS}$  reach high values of up to 30%. In addition to its chemical richness, the core shows a spatial molecular segregation with characteristic emission peaks of molecules, namely  $\text{c-C}_3\text{H}_2$ ,  $\text{CH}_3\text{OH}$ , and  $\text{HNCO}$  (Spezzano et al. 2017). These seem to be the emission peaks of several other species that are chemically related to the respective molecules: carbon-chain molecules are grouped in the south on the  $\text{c-C}_3\text{H}_2$  peak, O-bearing molecules such as  $\text{CH}_3\text{OH}$  or  $\text{SO}$  gather in the north-east on the  $\text{CH}_3\text{OH}$  peak, and  $\text{HNCO}$  in the north-west is joined by  $\text{CH}_3\text{CCH}$ . The spatial differentiation between carbon chains in the south and  $\text{CH}_3\text{OH}$  in the north has been explained by a non-uniform external illumination of the core (Spezzano et al. 2016). More precisely, L1544 is located at the edge of a filament in the Taurus molecular cloud, which leads to the southern part being exposed to the interstellar radiation field (ISRF), while the northern part is more protected by the molecular cloud. The ISRF drives the photochemistry in the south, enhancing the abundance of free carbon atoms in the gas phase, and subsequently the abundance of carbon chains. In the protected north,

however, photochemistry is not a dominant process, and carbon is mainly locked in CO. The northern part of the core is also known to be the meeting point of two filamentary structures (e.g. see [Spezzano et al. 2016](#); [Lin et al. 2022a](#)). [Giers et al. \(2025\)](#) suggest that inflowing, fresh material actually enhances the abundances of chemically young species in this area, causing the emission peak of CH<sub>3</sub>CCH in the north-west of the core.

This work focuses on the emission and the distribution of the two carbon chains HC<sub>3</sub>N and CH<sub>3</sub>CCH and their singly deuterated isotopologues. In L1544, the two molecules show a spatial differentiation (see Fig. 1), where the emission of HC<sub>3</sub>N follows other carbon chains and peaks in the south of the core, while CH<sub>3</sub>CCH peaks in the north-west on the HNCO peak. Therefore, the observations of HC<sub>3</sub>N, CH<sub>3</sub>CCH, and isotopologues offer complementary insights into the complex chemical structure of the prototypical pre-stellar core L1544. In addition, this dataset gives the opportunity to study the deuteration of larger molecules in L1544 in more detail, providing a deeper understanding of the chemical processes that dominate in pre-stellar cores and shape the observed chemical structures. In addition, the study of deuteration can help to better understand the formation pathways of the molecules and, eventually, put constraints on chemical models.

Cyanoacetylene, HC<sub>3</sub>N, is the smallest molecule from the family of cyanopolyyne, which are possible precursors of prebiotic molecules (see e.g. [Shingledecker et al. 2021](#)). After its first detection in space by [Turner \(1971\)](#), HC<sub>3</sub>N has since been detected in various interstellar environments (see e.g. [Morris et al. 1976](#); [Walmsley et al. 1980](#); [Chapillon et al. 2012](#); [Spezzano et al. 2017](#)). The deuterated counterpart, DC<sub>3</sub>N, was first detected by [Langer et al. \(1980\)](#) towards the low-mass dark cloud TMC-1, and by [Howe et al. \(1994\)](#) towards several other dark cores. Methylacetylene, CH<sub>3</sub>CCH, is a large carbon chain, and a proposed precursor in the formation of polycyclic aromatic hydrocarbons (PAHs) ([Parker & Kaiser 2017](#)). It contains a methyl group with three equivalent H atoms and one H atom in the terminal CCH group, which makes the study of its deuteration very useful for understanding the molecule's formation pathways. In the interstellar medium (ISM), CH<sub>3</sub>CCH was first detected by [Buhl & Snyder \(1973\)](#), followed by detections in various other environments ([van Dishoeck et al. 1995](#); [Fontani et al. 2002](#); [Vastel et al. 2014](#); [Gratier et al. 2016](#); [Spezzano et al. 2017](#); [Agúndez et al. 2019](#); [Lin et al. 2022b](#)). The singly deuterated isotopologues CH<sub>2</sub>DCCH and CH<sub>3</sub>CCD were first detected towards the cold dark cloud TMC-1 ([Gerin et al. 1992](#); [Markwick et al. 2005](#)). The detection of the doubly deuterated forms CHD<sub>2</sub>CCH and CH<sub>2</sub>DCCD was reported by [Agúndez et al. \(2021\)](#).

Both HC<sub>3</sub>N and CH<sub>3</sub>CCH are believed to primarily form in the gas phase. The main formation pathways for CH<sub>3</sub>CCH are thought to involve ion-molecule reactions, neutral-neutral reactions, and dissociative recombination of larger hydrocarbons ([Schiff & Bohme 1979](#); [Turner et al. 1999](#); [Calcutt et al. 2019](#); [Giers et al. 2025](#)), while for HC<sub>3</sub>N, potential formation routes are via HCN, CN, or HNC ([Iraqi et al. 1990](#); [Sims et al. 1993](#); [Fukuzawa & Osamura 1997](#); see [Hily-Blant et al. 2018](#) for an overview). Not much is known about the deuteration process of either species, but there is evidence that it occurs mainly in the gas phase. According to [Rivilla et al. \(2020\)](#), DC<sub>3</sub>N most likely forms via ion-molecule reactions, for example of HC<sub>3</sub>N directly reacting with H<sub>2</sub>D<sup>+</sup>, whereas the deuteration of CH<sub>3</sub>CCH is believed to occur via the dissociative recombination of C<sub>3</sub>H<sub>6</sub>D<sup>+</sup> and C<sub>3</sub>H<sub>5</sub>D<sup>+</sup> ([Agúndez et al. 2021](#)).

In this work, we present the emission maps of CH<sub>2</sub>DCCH, CH<sub>3</sub>CCD, and DC<sub>3</sub>N, and their non-deuterated isotopologues

CH<sub>3</sub>CCH, HC<sub>3</sub>N, and HCC<sup>13</sup>CN, observed towards the pre-stellar core L1544. We report the observations and detected lines in Sect. 2. In Sect. 3.2, we model spectral lines extracted towards the dust peak of the source with non-local thermodynamic equilibrium (non-LTE) radiative transfer calculations to constrain physical parameters of the molecular emission. Following this, we derive the corresponding column density and deuterium fraction maps of the different species in Sect. 3.3, assuming LTE conditions. In Sect. 4, we discuss the deuterium fractionation of HC<sub>3</sub>N and CH<sub>3</sub>CCH in L1544 and the implications for the understanding of the ongoing chemical processes. Section 5 concludes the article.

## 2. Data

The data presented in this work were taken with the IRAM 30 m single-dish radio telescope on Pico Veleta in the Sierra Nevada, Spain. The observations were carried out between October 2013 and June 2022 (PIs: Silvia Spezzano, Katharina Giers). The data for HC<sub>3</sub>N, HCC<sup>13</sup>CN, CH<sub>3</sub>CCH, and CH<sub>2</sub>DCCH have also been used in [Spezzano et al. \(2017\)](#) and [Giers et al. \(2025\)](#). The on-the-fly (OTF) maps were observed in position switching mode, using the EMIR E090 receiver and the Fourier transform spectrometer (FTS) backend with a spectral resolution of 50 kHz. The observed 2.5' × 2.5' OTF maps were centred on the source dust emission peak ( $\alpha_{2000} = 05^{\text{h}}04^{\text{m}}17^{\text{s}}.21$ ,  $\delta_{2000} = +25^{\circ}10'42''.8$ , [Ward-Thompson et al. 1999](#)). The observed transitions are summarised in Table 1.

Data processing was done using the GILDAS software ([Pety 2005](#)) and the python packages pandas ([Wes McKinney 2010](#)) and spectral-cube ([Ginsburg et al. 2019](#)). All emission maps were gridded to a pixel size of 8" with the CLASS software in the GILDAS packages. This corresponds to one-third to one-quarter of the actual beam size, depending on the frequency. To create a uniform dataset, we additionally resampled the data to a spectral resolution of 0.18 km s<sup>-1</sup>, corresponding to the resolution of the lowest frequency observation (84.4 GHz). The antenna temperature  $T_A^*$  was converted to the main beam temperature  $T_{\text{mb}}$  using the relation  $T_{\text{mb}} = F_{\text{eff}}/B_{\text{eff}} \cdot T_A^*$ . The corresponding values for the 30 m forward ( $F_{\text{eff}}$ ) and main-beam efficiencies ( $B_{\text{eff}}$ ) are given in Table 1. Figure 1 shows the integrated intensity maps of the observed transitions, computed by integrating over a velocity range of 0.7 km s<sup>-1</sup> around each line. For CH<sub>3</sub>CCH, only the K=0 and K=1 transitions were considered, due to the low signal-to-noise ratio of the K=2 and K=3 transitions. To enable comparison between the molecules in our following analysis, all maps were convolved to an angular resolution of 31", which corresponds to the half-power beam width (HPBW) of the largest observed beam.

## 3. Analysis

### 3.1. Spectral line emission

The goal of this work is to study the deuterium fraction of HC<sub>3</sub>N and CH<sub>3</sub>CCH across the source. To do so, a reliable estimation of the molecular column densities is crucial.

For CH<sub>3</sub>CCH and CH<sub>3</sub>CCD, we observe more than one transition. Figure 2 presents spectra of the CH<sub>3</sub>CCH (5–4) and (6–5), and the CH<sub>3</sub>CCD (6–5) K=0 and K=1 transitions, extracted towards the three molecular peaks and the dust peak in L1544 by using a circular aperture with a diameter corresponding to the telescope beam size, 31". The extraction locations and beam size are indicated in Fig. 1. The observations show

Table 1: Spectroscopic parameters of the observed lines.

Molecule	Transition ( $J'_{K'} - J_K$ )	Frequency <sup>a</sup> (MHz)	$F_{\text{eff}}/B_{\text{eff}}$	rms (mK)	$E_{\text{up}}^a$ (K)	$g_{\text{up}}^a$	$A^a$ ( $\text{s}^{-1}$ )	Reference
$\text{HC}_3\text{N}$	$J = 11 - 10$	100076.39(2)	0.95/0.79	110	28.8	23	$7.77 \times 10^{-5}$	1
$\text{HCC}^{13}\text{CN}^*$	$J = 10 - 9$	90601.78(3)	0.95/0.80	8	23.9	21	$5.74 \times 10^{-5}$	2
$\text{DC}_3\text{N}^*$	$J = 10 - 9$	84429.814(3)	0.95/0.81	17	22.3	21	$4.69 \times 10^{-5}$	1
$\text{DC}_3\text{N}$	$J = 11 - 10$	92872.375(3)	0.95/0.80	19	26.7	23	$6.24 \times 10^{-5}$	1
$\text{CH}_3\text{CCH}$	$J_K = 5_3 - 4_3$	85442.6012(1)	0.95/0.81	16	77.3	44	$1.30 \times 10^{-6}$	3
$\text{CH}_3\text{CCH}$	$J_K = 5_2 - 4_2$	85450.7663(1)	0.95/0.81	16	41.1	22	$1.70 \times 10^{-6}$	3
$\text{CH}_3\text{CCH}^*$	$J_K = 5_1 - 4_1$	85455.6667(1)	0.95/0.81	10	19.5	22	$1.95 \times 10^{-6}$	3
$\text{CH}_3\text{CCH}$	$J_K = 5_0 - 4_0$	85457.3003(1)	0.95/0.81	10	12.3	22	$2.03 \times 10^{-6}$	3
$\text{CH}_3\text{CCH}$	$J_K = 6_3 - 5_3$	102530.3476(1)	0.95/0.79	37	82.3	52	$2.69 \times 10^{-6}$	3
$\text{CH}_3\text{CCH}$	$J_K = 6_2 - 5_2$	102540.1446(1)	0.95/0.79	37	46.1	26	$3.16 \times 10^{-6}$	3
$\text{CH}_3\text{CCH}$	$J_K = 6_1 - 5_1$	102546.0242(1)	0.95/0.79	37	24.5	26	$3.46 \times 10^{-6}$	3
$\text{CH}_3\text{CCH}$	$J_K = 6_0 - 5_0$	102547.9844(1)	0.95/0.79	33	17.2	26	$3.56 \times 10^{-6}$	3
$\text{CH}_3\text{CCD}$	$J_K = 6_1 - 5_1$	93454.331(3)	0.95/0.80	8	22.9	26	$2.51 \times 10^{-6}$	4
$\text{CH}_3\text{CCD}^*$	$J_K = 6_0 - 5_0$	93456.044(3)	0.95/0.80	8	15.7	26	$2.59 \times 10^{-6}$	4
$\text{CH}_2\text{DCCH}^*$	$J_{K_a K_c} = 6_{06} - 5_{05}$	97080.728(6)	0.95/0.80	15	16.3	13	$3.03 \times 10^{-6}$	4

**Notes.** The transitions used to derive the molecular column density are marked with an asterisk. Numbers in parenthesis give the uncertainty on the last digit. <sup>(a)</sup> Extracted from the Cologne Database for Molecular Spectroscopy (Müller et al. 2001).

**References.** (1) Mallinson & de Zafra (1978), (2) Creswell et al. (1977), (3) Bauer & Burie (1969), (4) Leguenec et al. (1993).

that the line intensity ratio between the  $K=0$  and  $K=1$  transitions varies across the core, for  $\text{CH}_3\text{CCH}$  between 1:1 and 1:1.2, and for  $\text{CH}_3\text{CCD}$  between 1:1 and 1:1.4. In a first approach, we assumed local thermodynamic equilibrium (LTE) and modelled the spectra using `lte_molecule` and `generate_model` from the python package `pyspeckit`. We applied a constant excitation temperature of 10 K, which is consistent with previous measurements of  $\text{CH}_3\text{CCH}$  in this source (e.g. Vastel et al. 2014), and adjusted the column densities to fit the intensity of the  $K=0$  lines. The resulting modelled spectra are shown in red in Fig. 2. For both  $\text{CH}_3\text{CCH}$  and  $\text{CH}_3\text{CCD}$ , the line ratio between  $K=0$  and  $K=1$  is estimated to be around 2:1. This is not visible in the observations, which vary between 1:1 and 1:1.4. However, the emission lines are in the optically thin regime, with  $\tau_{\text{max}}(T_{\text{ex}} = 10 \text{ K}) \approx 0.27$ . Therefore, self-absorption is unlikely to be the cause of the line ratios. Following this, there must be another effect influencing the line intensities, and given the relatively high critical density of  $\text{CH}_3\text{CCH}$  ( $n_{\text{crit}} \approx 10^5 \text{ cm}^{-3}$ ) compared to the densities across the core ( $10^4 - 10^7 \text{ cm}^{-3}$ ), it is likely that non-LTE effects play a role.

Therefore, a non-LTE approach would be necessary to test whether non-LTE effects might cause the observed intensity ratios, and to constrain the molecular column densities. A full non-LTE analysis lies beyond the scope of this paper, because the required 3D model of the temperature and density structure of the core does not exist. Instead, we focus on the analysis of the emission lines extracted at the dust peak of L1544. In the following, we model the observed spectra with non-LTE radiative transfer in Sec. 3.2, before we analyse the column densities and deuterium fractions in LTE in Sec. 3.3, using the non-LTE results to constrain the physical parameters of the emission.

### 3.2. Non-LTE modelling at the dust peak

In this section, we simulate the observed molecular spectra towards the dust peak of L1544 with the non-LTE radiative

transfer code Line Transfer with OpenCL (LOC, Juvela 2020). We assumed a 1D model that considers spherical symmetry of the physical properties and chemical abundances. The physical structures are characterised by volume density, kinetic temperature, and infall velocity. For this, we adopted the physical model of L1544 presented in Keto et al. (2015) (hereafter Keto-Caselli model), shown in Fig. 3. It describes an unstable quasi-equilibrium Bonnor-Ebert sphere (Ebert 1955; Bonnor 1956) with a peak central  $\text{H}_2$  volume density of  $n_0 \approx 10^7 \text{ cm}^{-3}$  and a central gas temperature of 6 K. To approximate the molecular abundances, we used profiles of the fractional abundance with respect to  $\text{H}_2$  molecules, hereafter referred to as 'abundance profiles'. We applied both constant abundance profiles, as well as radial abundance profiles predicted by the state-of-the-art gas-grain chemical model `pyRate` (Sipilä et al. 2019). For the constant abundance profiles, we set the abundance to zero within a radius of 1800 au, as L1544 is known to exhibit a freeze-out of 99.99% of species heavier than Helium in this central region (Caselli et al. 2022). In `pyRate`, we applied the two-phase model of the code, where the gas-phase chemistry and the entire ice chemistry on the grains are active. We used the same initial abundances and chemical networks as presented in Sipilä et al. (2019) and the same standard values for various model parameters as used in Giers et al. (2022). In the chemical simulation, the Keto-Caselli model is used as a static physical model for L1544, assuming an external visual extinction of  $A_V = 2 \text{ mag}$  to account for the molecular cloud where the core is embedded. The resulting abundance profiles were extracted at various evolutionary times across the chemical simulation.

For the line simulations of  $\text{HC}_3\text{N}$  and  $\text{CH}_3\text{CCH}$ , the latest collision rate coefficients are available on the Leiden Atomic and Molecular Database (LAMDA, Schöier et al. 2005; Faure et al. 2016; Ben Khalifa et al. 2024). In the case of  $\text{HCC}^{13}\text{CN}$ , we used the rates of  $\text{HC}_3\text{N}$  and scaled them with the corresponding reduced mass of the isotopologue. For the deuterated isotopologues of  $\text{HC}_3\text{N}$  and  $\text{CH}_3\text{CCH}$ , a scaling of the rates was not

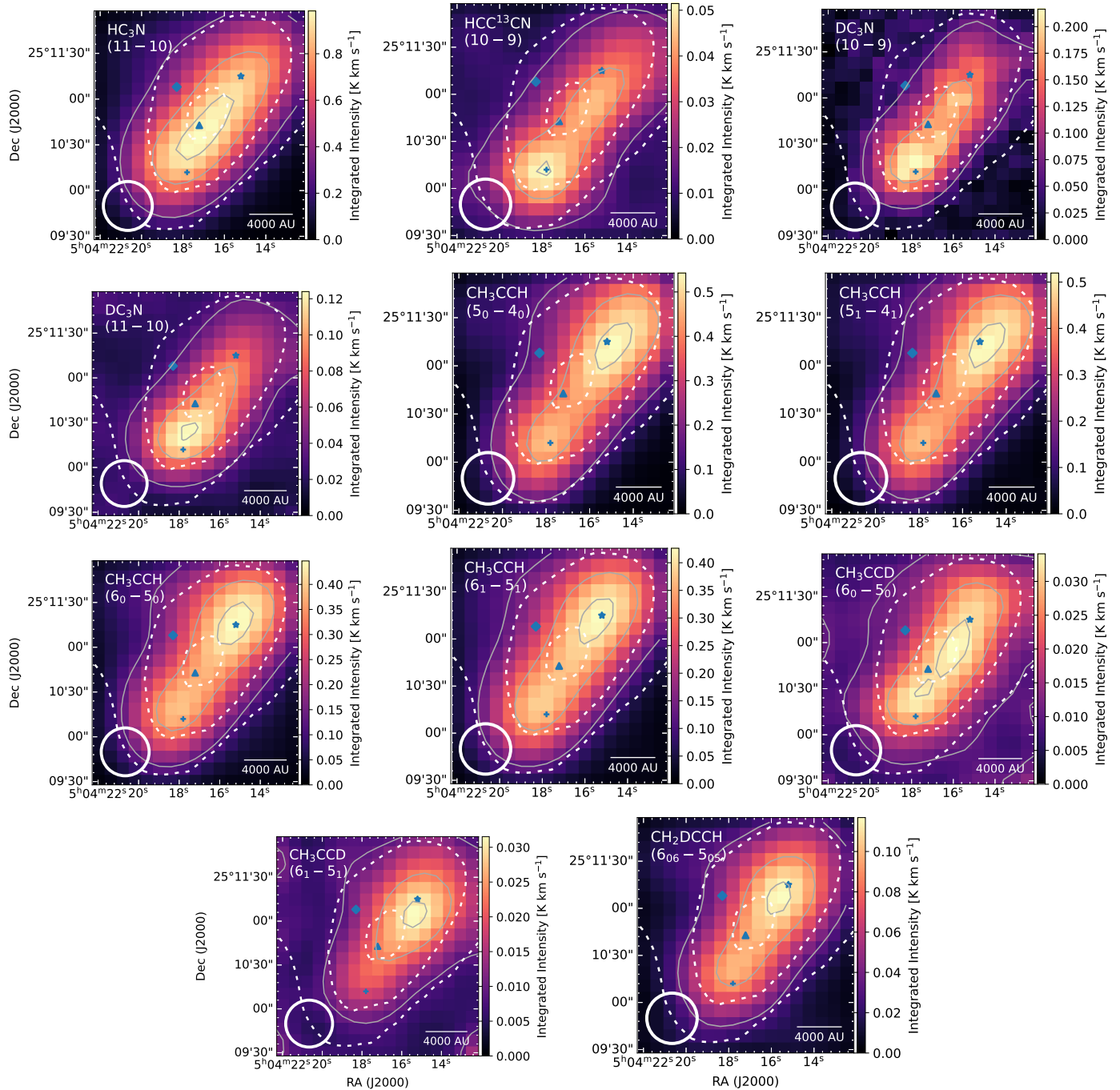


Fig. 1: Integrated intensity maps of the observed transitions. The grey solid line contours indicate the 30%, 70%, and 90% level of the peak integrated intensity. The dashed line contours represent 30%, 50%, and 90% of the  $\text{H}_2$  column density peak derived from *Herschel* maps (Spezzano et al. 2016). The markers in blue represent the dust peak (triangle) and the molecular emission peaks of  $\text{CH}_3\text{OH}$  (diamond),  $\text{CH}_3\text{CCH}$  (star), and  $\text{c-C}_3\text{H}_2$  (plus sign), where emission spectra (shown in Fig. 2) are extracted within a circular aperture with a diameter corresponding to the telescope beam. The white circle in the bottom-left corner indicates the beam size of the IRAM 30 m telescope (31'').

possible, as the different nuclear spins induce different hyperfine structures. Therefore, we could not apply the non-LTE modelling to these species.

The abundance profiles that provide the best-fit solutions for  $\text{HC}_3\text{N}$  and  $\text{CH}_3\text{CCH}$  are shown in Fig. 4. A comparison between the modelled spectra and the observed lines is shown in Fig. 5 for  $\text{HC}_3\text{N}$ , and  $\text{HCC}^{13}\text{CN}$ , and in Fig. 6 for  $\text{CH}_3\text{CCH}$ . The observed spectra, shown in black, are extracted at the dust peak of

the core, averaged over an area corresponding to the telescope beam size (31''). To enable a comparison, the synthetic spectra were convolved with this observational beam for each transition frequency. The molecular column densities at the dust peak derived by LOC are given in Table 2.

The spectrum of  $\text{HCC}^{13}\text{CN}$  can be reproduced both with a constant abundance and a radial abundance profile from the chemical modelling. With a depletion radius of 1800 au, a con-

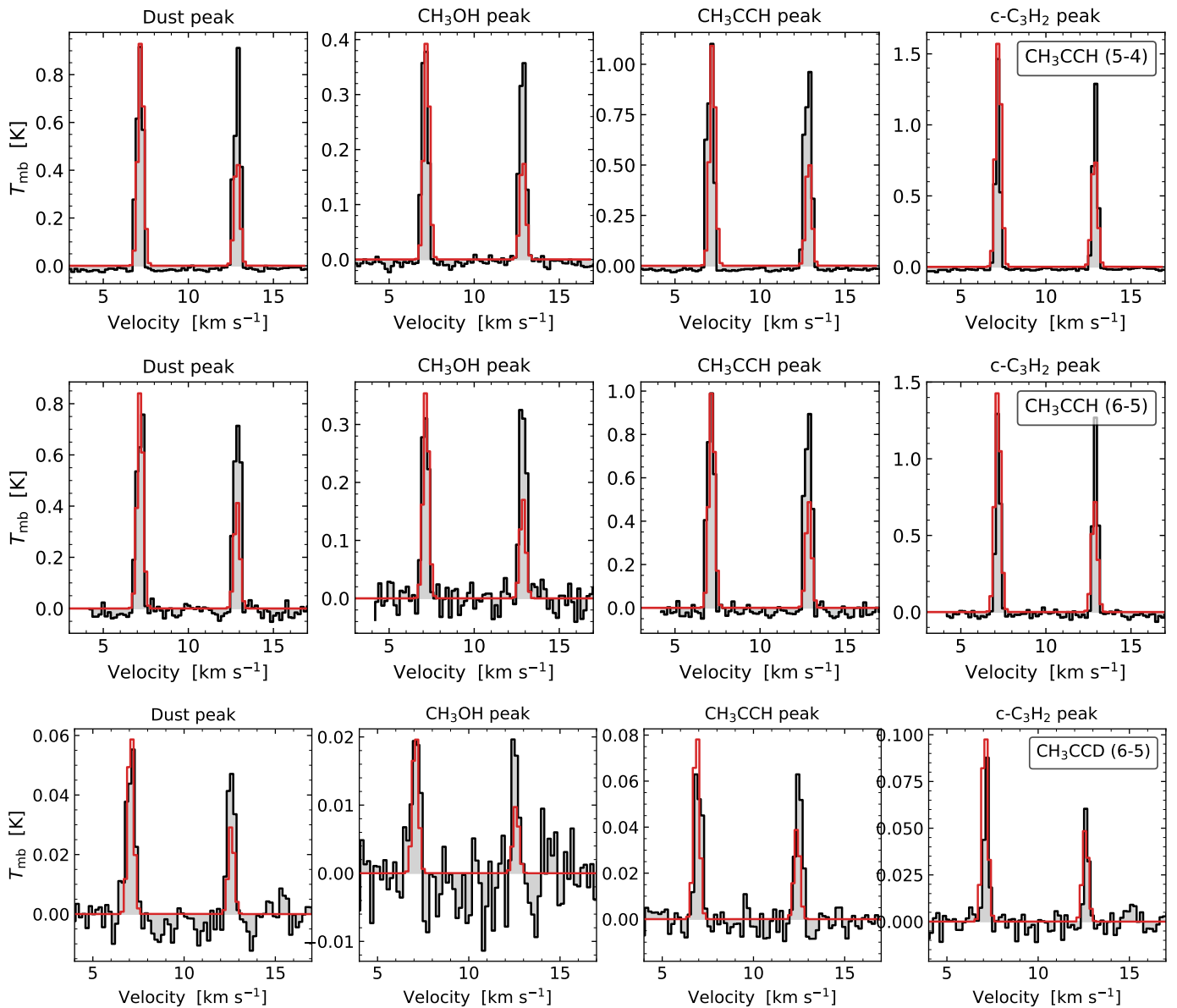


Fig. 2: Observed spectra (black) of the  $\text{CH}_3\text{CCH}$  (top) and the  $\text{CH}_3\text{CCD}$  (bottom)  $K=0$  and  $K=1$  transitions extracted towards the three molecular peaks in L1544 and the dust peak, using a circular aperture with diameter  $31''$ . The extraction locations are indicated in Fig. 1. Shown in red are synthetic spectra produced with the LTE model generator of the python package `pyspeckit`. The input column densities are  $[4, 2, 5, 8](\pm 0.3) \times 10^{15} \text{ cm}^{-2}$  for  $\text{CH}_3\text{CCH}$  and  $[3, 1, 4, 5](\pm 0.3) \times 10^{12} \text{ cm}^{-2}$  for  $\text{CH}_3\text{CCD}$  at the dust peak,  $\text{CH}_3\text{OH}$  peak,  $\text{CH}_3\text{CCH}$  peak, and  $\text{c-C}_3\text{H}_2$  peak, respectively. The input excitation temperature is set to a constant value of 10 K for both molecules.

stant abundance of  $2.5 \cdot 10^{-11}$  fits best. When applying the abundance profiles from `pyRate`, the observed lines are reproduced within a factor of 2 with profiles extracted at early time steps of the chemical simulation ( $t_1 = 10^5$  yrs,  $t_2 = 1.3 \cdot 10^5$  yrs).

The brightness of the  $\text{HC}_3\text{N}$  spectral line can be reproduced with modelling at a constant fractional abundance of  $1.5 \cdot 10^{-9}$  with a depletion radius of 1800 au, and, similar to  $\text{HCC}^{13}\text{CN}$ , at early time steps within a factor of 2 in intensity ( $t_1 = 10^5$  yrs,  $t_2 = 1.3 \cdot 10^5$  yrs). However, the modelling fails to recreate the slightly asymmetric, redshifted shape of the line profile. This asymmetric shape is likely caused by the velocity gradient across the core with higher velocities in the south, where  $\text{HC}_3\text{N}$  peaks (Bianchi et al. 2023). Therefore, more material emits at slightly higher velocities, compared to the systemic velocity of the core in the

centre, causing a redshifted asymmetry. The column densities of  $\text{HC}_3\text{N}$  and  $\text{HCC}^{13}\text{CN}$  derived by the best-fit models result in an isotopic ratio of  $^{12}\text{C}/^{13}\text{C} = 60 \pm 20$ , which is in agreement with the value for the local interstellar medium,  $^{12}\text{C}/^{13}\text{C} = 68$  (Milam et al. 2005).

All observed transitions of  $\text{CH}_3\text{CCH}$  can be reproduced with a constant abundance profile of  $1.5 \cdot 10^{-9}$  and a depletion radius of 1800 au. As the non-LTE modelling is able to reproduce the observed line ratios between the  $K=0$  and  $K=1$  transitions correctly, we are able to use the central column density of  $\text{CH}_3\text{CCH}$  derived by LOC in the analysis below. However, the emission lines cannot be reproduced with any of the abundance profiles derived from chemical modelling. In fact, the radially varying abundance profiles largely underestimate the abundance

of  $\text{CH}_3\text{CCH}$ , by roughly three orders of magnitude. Figure 6 illustrates that it is necessary to multiply the abundance profile by a factor of 700 to reproduce the observed line intensities. This issue was already noted in previous research, where various chemical models failed to predict observed molecular abundances of  $\text{CH}_3\text{CCH}$ . The formation pathways of  $\text{CH}_3\text{CCH}$  have been widely studied, with formation proposed via ion-molecule reactions, neutral-neutral reactions, and dissociative recombination in the gas phase (Schiff & Bohme 1979; Turner et al. 1999; Calcutt et al. 2019), and hydrogenation of  $\text{C}_3$  on grain surfaces (Hickson et al. 2016; Guzmán et al. 2018). However, models demonstrated that these gas-phase and grain-surface formation pathways are not sufficient to reproduce  $\text{CH}_3\text{CCH}$  abundances in cold molecular clouds (see e.g. Öberg et al. 2013; Hickson et al. 2016). Hence, it is necessary to further investigate potential grain surface reactions of  $\text{CH}_3\text{CCH}$  or alternative gas phase pathways at low temperatures to improve the chemical networks and ultimately the model predictions.

Table 2: Molecular column densities for the best-fit models, derived with LOC towards the dust peak (see Figs. 5 and 6).

Molecule	model	$N^{\text{NLTE}}$ ( $\times 10^{12} \text{ cm}^{-2}$ )
$\text{HC}_3\text{N}$	const	38
	radial ( $t_1$ )	64
	radial ( $t_2$ )	21
$\text{HCC}^{13}\text{CN}$	const	0.63
	radial ( $t_1$ )	0.94
	radial ( $t_2$ )	0.31
$\text{CH}_3\text{CCH}$	const	45

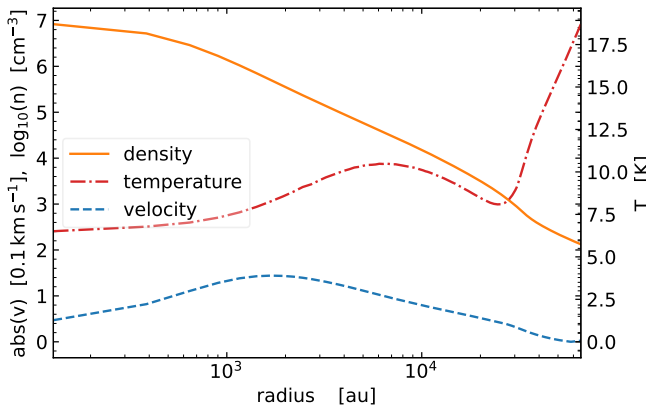


Fig. 3: Profiles of the gas temperature (red),  $\text{H}_2$  number density (orange, in logarithmic scale), and infall velocity (blue, in units of  $0.1 \text{ km s}^{-1}$ ) for the Keto-Caselli model of L1544 (Keto et al. 2015). The velocity in the model is negative but is shown here as positive to improve readability.

### 3.3. Column density and deuteration maps

A detailed non-LTE analysis is only possible towards the dust peak of L1544. To study the distribution of the molecular emission across the core, we used the LTE assumptions to compute

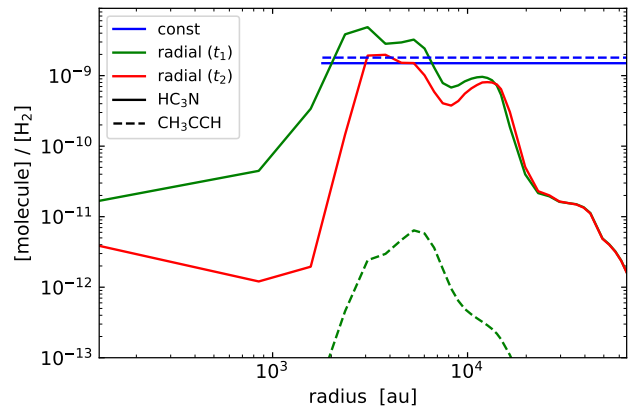


Fig. 4: Fractional abundance profiles of  $\text{HC}_3\text{N}$  (solid) and  $\text{CH}_3\text{CCH}$  (dashed) of the best-fit results produced with LOC. For  $\text{HCC}^{13}\text{CN}$ , the radial abundance profiles derived with chemical modelling (green, red) correspond to the profiles of the main isotopologue, scaled down by the isotopic ratio, 68.

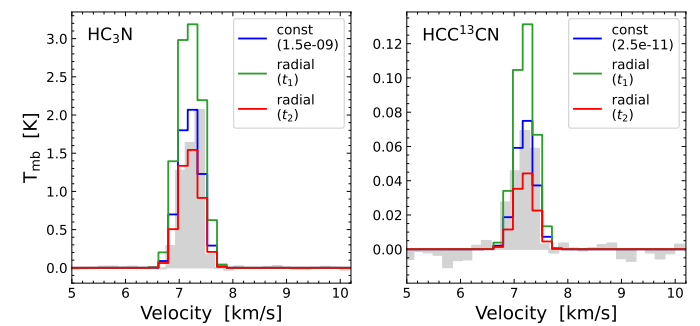


Fig. 5: Comparison of the observed spectra (grey) of  $\text{HC}_3\text{N}$ , and  $\text{HCC}^{13}\text{CN}$ , extracted towards the dust peak of L1544, to the synthetic spectra (red, blue, green) produced with LOC. For the constant abundances, a depletion radius of 1800 au is assumed.

the column density maps, and used the non-LTE results as a constraint.

#### 3.3.1. Column density

To derive the molecular column densities, we assumed optically thin emission, following the derivation presented in Mangum & Shirley (2015). Furthermore, we applied the approximation of a constant excitation temperature across the core (see Caselli et al. 2002b; Redaelli et al. 2019). This results in a column density of

$$N = \frac{8\pi\nu^3}{c^3} \frac{Q_{\text{rot}}(T_{\text{ex}})}{g_u A_{\text{ul}}} \left[ J_{\nu}(T_{\text{ex}}) - J_{\nu}(T_{\text{bg}}) \right]^{-1} \frac{e^{\frac{E_u}{kT_{\text{ex}}}}}{e^{\frac{h\nu}{kT_{\text{ex}}}} - 1} \int T_{\text{mb}} dv, \quad (2)$$

where  $Q_{\text{rot}}(T_{\text{ex}})$  is the partition function of the molecule at an excitation temperature  $T_{\text{ex}}$ ,  $g_u$  and  $E_u$  respectively represent the degeneracy and energy of the upper level of the transition,  $A_{\text{ul}}$  is the Einstein coefficient for spontaneous emission,  $T_{\text{bg}} = 2.73 \text{ K}$  is the temperature of the cosmic microwave background,  $J(T)$  is the Rayleigh-Jeans equivalent temperature, and  $T_{\text{mb}}$  is the main-beam temperature. The corresponding parameters for each transition used in the derivation of the column density are listed in Table 1.

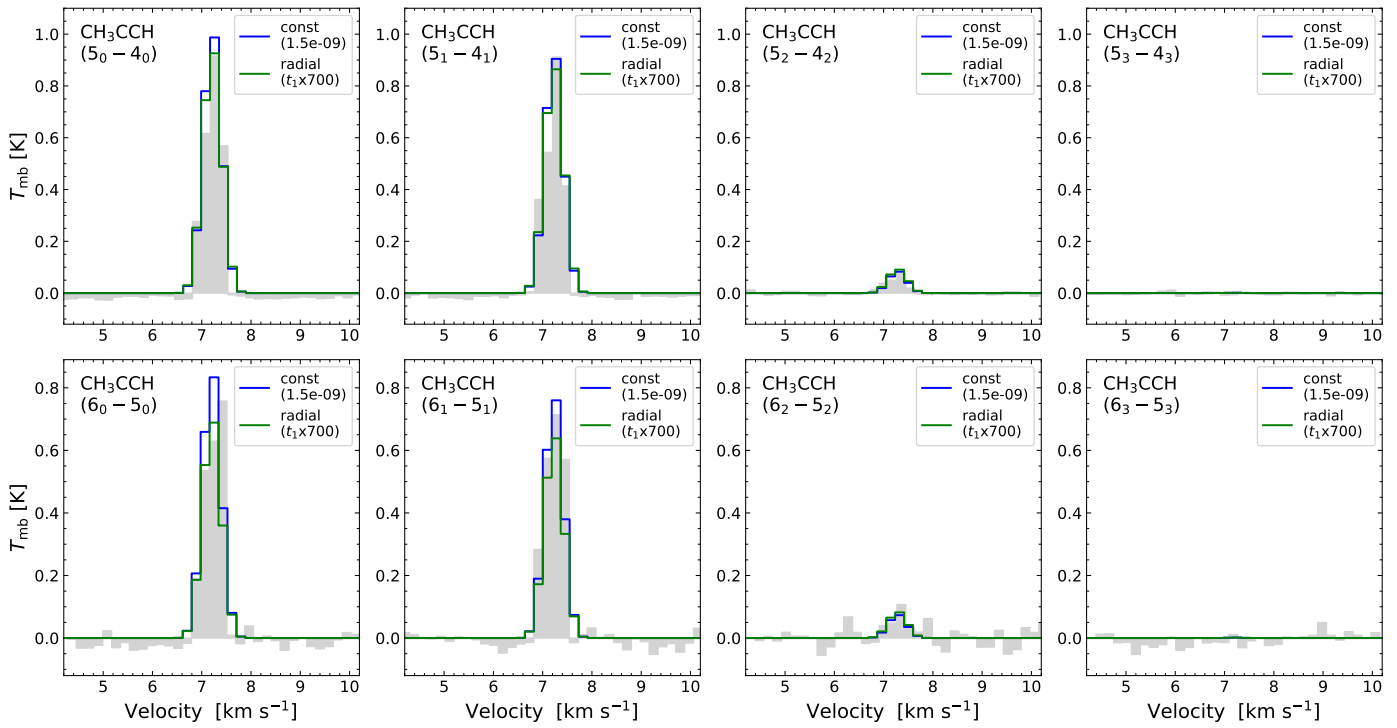


Fig. 6: Comparison of the observed spectra (grey) of  $\text{CH}_3\text{CCH}$ , extracted towards the dust peak of L1544, to the synthetic spectra (red, blue, green) produced with LOC. For the constant abundances, a depletion radius of 1800 au is assumed.

The observed range of  $E_u$  only covers about 5 K for the molecules where multiple transitions were observed ( $\text{CH}_3\text{CCH}$ ,  $\text{CH}_3\text{CCD}$ ,  $\text{DC}_3\text{N}$ ). Therefore, an excitation analysis to derive the excitation temperatures pixel by pixel is not feasible. Instead, we followed Redaelli et al. (2019) to determine the excitation temperatures for  $\text{CH}_3\text{CCH}$  and  $\text{HCC}^{13}\text{CN}$  and fixed the column density at the dust peak to the value derived from a constant molecular abundance profile with the non-LTE modelling in Sect. 3.2 (see Table 2). From this, we derived the corresponding excitation temperatures in the LTE regime, using Eq. 2, and applied this value across the whole core to derive the column density maps.

Therefore, we set an excitation temperature of 7 K for  $\text{HCC}^{13}\text{CN}$  and 10 K for  $\text{CH}_3\text{CCH}$ , which is in agreement with values used in previous studies (see e.g. Howe et al. 1994; Markwick et al. 2005; Vastel et al. 2014; Hily-Blant et al. 2018; Agúndez et al. 2019; Bianchi et al. 2023). As shown in the previous section, non-LTE effects are responsible for the line intensity ratio observed for  $\text{CH}_3\text{CCH}$  K=0 and K=1 towards the dust peak. We decided to use the K=0 lines to derive the column density map for  $\text{CH}_3\text{CCH}$ , because the column density value of these lines at the dust peak matches with an excitation temperature that is reasonable for L1544. For the K=1 lines, however, we would have to use an excitation temperature around 60 K, which is significantly higher than what was routinely observed in this core. An example of the  $\text{CH}_3\text{CCH}$  column density and deuteration maps derived from the K=1 transitions is given in Appendix A.2. For the further analysis, we focus on the K=0 line of the (5-4) transition instead of the (6-5) transition because of its higher signal-to-noise ratio.

As the non-LTE approach was not possible for the deuterated isotopologues due to missing collision rate coefficients, we adopted the respective excitation temperature of the main species. To derive the column density of  $\text{CH}_3\text{CCD}$ , we used the

K=0 transition, as for  $\text{CH}_3\text{CCH}$ . The effect of the excitation temperature on the derived column density ratios was found to be weak, with a change of a few percent upon a variation of  $\pm 1$  K (as stated in Spezzano et al. 2013).

To account for the varying optical depth of the lines across the core, we corrected the column density by deriving the optical depth at each pixel individually using the respective excitation temperature, then multiplying the maps by (see e.g. Goldsmith & Langer 1999)

$$f_\tau = \frac{\tau}{1 - e^{-\tau}}. \quad (3)$$

This results in a correction factor of up to 1.1 in the southern part of the core.

The transitions used to derive the column density for each species are marked with an asterisk in Table 1. The corresponding column density maps are presented in Fig. 7. In the following, we discuss the results for the each species individually.

$\text{HC}_3\text{N}$ : The emission of  $\text{HC}_3\text{N}$  is moderately thick in this core, with optical depths of up to 0.9. Therefore, we approximated the column density of  $\text{HC}_3\text{N}$  with the emission of the  $^{13}\text{C}$  isotopologue, multiplied by the isotopic ratio for the local interstellar medium,  $^{12}\text{C}/^{13}\text{C} = 68$ . Given the results of the non-LTE modelling,  $^{12}\text{C}/^{13}\text{C} = 60 \pm 20$  at the dust peak, this is a reasonable assumption. The resulting column density map peaks in the south-east of the core (see Fig. 7), on the carbon-chain peak caused by non-uniform external illumination (see Spezzano et al. 2017), with a maximum value of  $6.3(5) \times 10^{13} \text{ cm}^{-2}$ , where the number in parenthesis indicates the uncertainty of the last digit. This is consistent with previous measurements towards L1544 ( $2.8 \times 10^{13} \text{ cm}^{-2}$ , Hily-Blant et al. 2018;  $7(2) \times 10^{13} \text{ cm}^{-2}$ , Howe et al. 1994). Additionally, the column density of  $\text{HC}_3\text{N}$  shows a local peak towards the north-west of the core (where

$\text{CH}_3\text{CCH}$  peaks) with a maximum of  $5.4(5) \times 10^{13} \text{ cm}^{-2}$ , and a dip in the core centre indicating the molecular freeze-out zone. The deuterated isotopologue is distributed similarly to the  $^{13}\text{C}$ -isotopologue, peaking in the south-east ( $3.5(2) \times 10^{12} \text{ cm}^{-2}$ ), and with a local peak in the north-west ( $3.1(2) \times 10^{12} \text{ cm}^{-2}$ ). These column density levels are consistent with previous measurements towards L1544 (e.g. Howe et al. 1994).

$\text{CH}_3\text{CCH}$ : In contrast to  $\text{HC}_3\text{N}$ , the emission of  $\text{CH}_3\text{CCH}$  peaks in the north-west of the core, with a maximum value of  $5.85(6) \times 10^{13} \text{ cm}^{-2}$ . Here, it is possible that ongoing accretion of material from cloud to core leads to chemically fresh gas and a replenishment of  $\text{CH}_3\text{CCH}$  (see Giers et al. 2025). A weaker, secondary peak is visible in the south-east of the core, on the carbon-chain peak, with values of  $5.43(6) \times 10^{13} \text{ cm}^{-2}$ . The column density of  $\text{CH}_2\text{DCCH}$  is distributed similarly to the main isotopologue, with a peak column density of  $2.0(2) \times 10^{13} \text{ cm}^{-2}$  and a southern peak at  $1.7(2) \times 10^{13} \text{ cm}^{-2}$ , which is equal to the northern peak within error bars. The column density of  $\text{CH}_3\text{CCD}$ , on the other hand, peaks closer to the core centre ( $4.1(4) \times 10^{12} \text{ cm}^{-2}$ ), with a second, equally strong peak ( $4.0(5) \times 10^{12} \text{ cm}^{-2}$ ) in the southern part of the core.

### 3.3.2. Deuterium fraction

The deuterium fractions were derived pixel by pixel by dividing the column density maps of the deuterated isotopologues by the column density map of the corresponding main species. For the ratio of  $\text{N}(\text{CH}_2\text{DCCH})/\text{N}(\text{CH}_3\text{CCH})$ , we accounted for the degeneracy of the D atom by dividing the ratio by a factor of 3. The resulting deuterium maps are presented in Fig. 8 for  $\text{HC}_3\text{N}$ , and Fig. 9 for  $\text{CH}_3\text{CCH}$ . In the following, we describe the results for each molecule individually:

$\text{DC}_3\text{N}/\text{HC}_3\text{N}$ : The deuterium fraction map shows moderate levels of deuteration, in the range of 0.04 - 0.07. The distribution is rather homogeneous across the whole core. The highest values (0.06-0.07) are widespread, and located mostly north and south-east of the core centre.

$\text{CH}_3\text{CCD}/\text{CH}_3\text{CCH}$ : The map shows that the deuterium fraction is, within the uncertainties (see Fig. A.1), distributed rather homogeneously across the core, with values between 0.07 and 0.09. A trend of higher values ( $\geq 0.09$ ) is visible towards the centre and the north-east of the core. The high D/H values at the edges of the map should be treated with caution since they have large uncertainties of around 30%.

$\text{CH}_2\text{DCCH}/\text{CH}_3\text{CCH}$ : This deuterium map shows a larger extension across the core than the map of  $\text{CH}_3\text{CCD}/\text{CH}_3\text{CCH}$ , due to a better signal-to-noise ratio. Additionally, the map exhibits a significantly higher deuterium fraction than  $\text{CH}_3\text{CCD}/\text{CH}_3\text{CCH}$ , with values between 0.09 and 0.15. In contrast to  $\text{CH}_3\text{CCD}/\text{CH}_3\text{CCH}$ , the distribution of  $\text{CH}_2\text{DCCH}/\text{CH}_3\text{CCH}$  exhibits a clear peak away from the centre towards the north-east of the core, with a peak value of 0.15(3).

$\text{CH}_2\text{DCCH}/\text{CH}_3\text{CCD}$ : The ratio map between the two deuterated isotopologues shows that  $\text{CH}_2\text{DCCH}$  is more abundant than  $\text{CH}_3\text{CCD}$ . The distribution is roughly homogeneous across the

core, with a slight trend of higher values towards the north ( $5.3 \pm 0.9$ ) compared to the south ( $4.1 \pm 0.9$ ). The statistically expected ratio of  $\text{CH}_2\text{DCCH}/\text{CH}_3\text{CCD}$  is 3, which results from the statistical considerations for the insertion of deuterium in the  $\text{CH}_3$  group and the CCH group. We derive an average ratio of 4.5(8), which is a 50% increase with respect to the statistical value.

## 4. Discussion

### 4.1. $\text{HC}_3\text{N}$

The column density maps presented in Fig. 7 show that the two carbon chains  $\text{HC}_3\text{N}$  and  $\text{CH}_3\text{CCH}$  and their deuterated counterparts exhibit different morphologies across the core. The emission of both  $\text{HC}_3\text{N}$  and its deuterated isotopologue peak at the carbon-chain peak in the south of the core. The resulting deuterium fraction map, however, exhibits a rather homogeneous distribution across the core with moderate levels of deuteration (0.05-0.07). This is in agreement with previous measurements in L1544 (Howe et al. 1994). Results for the deuterium fraction of  $\text{HC}_3\text{N}$  show roughly similar values in other cores: 0.03-0.11 in the dark cloud TMC-1 (Howe et al. 1994), 0.03(1) in the cold envelope of the Class 0 protostar L1527 (Sakai et al. 2009), and 0.03(1) in the dense core L483 (Turner 2001; Sakai et al. 2009; Agúndez et al. 2019).

The moderate deuteration levels and extended morphology of the deuteration map in L1544 indicate that  $\text{HC}_3\text{N}$  and  $\text{DC}_3\text{N}$  do not trace the high-density regions in the core centre (e.g.  $\text{N}_2\text{H}^+$  and  $\text{N}_2\text{D}^+$ ), but rather a less dense layer of gas in an outer shell of the core (in agreement with Rivilla et al. 2020), at densities of less than  $10^5 \text{ cm}^{-3}$  (see Fig. 4). In the less dense gas, the process of deuteration is less efficient due to a lower abundance of  $\text{H}_2\text{D}^+$ . Therefore, the moderate deuterium fraction suggests that  $\text{DC}_3\text{N}$  is most likely formed in the gas phase, presumably via ion-molecule reactions, as discussed in Rivilla et al. (2020).

The assumption that  $\text{HC}_3\text{N}$  and  $\text{DC}_3\text{N}$  trace intermediate-density gas in L1544 is supported by the abundance profiles used to reproduce the emission lines of  $\text{HC}_3\text{N}$  and  $\text{HCC}^{13}\text{CN}$  (see Fig. 4). These abundance profiles peak at a volume density of roughly  $10^5 \text{ cm}^{-3}$ , which is significantly lower than the critical densities of both transitions ( $n_{\text{crit}}(\text{HC}_3\text{N}) \approx 10^7 \text{ cm}^{-3}$ ,  $n_{\text{crit}}(\text{HCC}^{13}\text{CN}) \approx 10^6 \text{ cm}^{-3}$ ). This was also observed by Bianchi et al. (2023), who state that the carbon-chain abundance is enhanced towards the external part of the core, where the material is more exposed to the ISRF (see also Spezzano et al. 2016). This becomes visible in the slightly asymmetric line shapes of  $\text{HC}_3\text{N}$  and  $\text{HCC}^{13}\text{CN}$  at the dust peak and the c- $\text{C}_3\text{H}_2$  peak (see Fig. B.1). This asymmetry is caused by the velocity gradient across L1544, which leads to higher velocities at the carbon-chain peak in the southern part (see Spezzano et al. 2016, 2017; Giers et al. 2025), creating redshifted, asymmetric line profiles for carbon-chain molecules, as most of their emission originates in this part. This effect cannot be reproduced with non-LTE modelling, because the physical structure assumes the core to be spherically symmetric and does not account for asymmetric velocity variations across the core.

### 4.2. $\text{CH}_3\text{CCH}$

The observed ratios between the peak intensities of the K=0 and K=1 emission lines of  $\text{CH}_3\text{CCH}$  and  $\text{CH}_3\text{CCD}$  – both for the (5–4) and the (6–5) transitions – cannot be reproduced assuming LTE conditions but instead require a non-LTE treatment. Com-

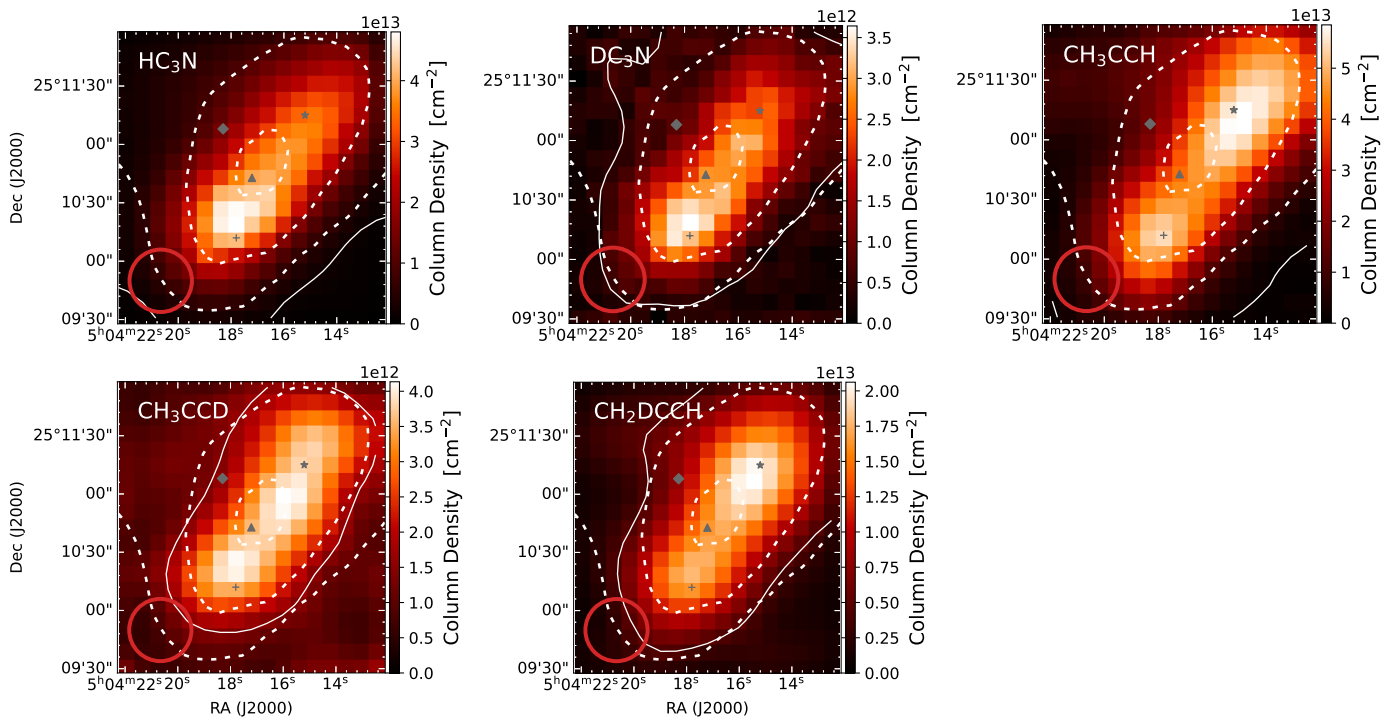


Fig. 7: Column density maps of  $\text{HC}_3\text{N}$  and  $\text{CH}_3\text{CCH}$  and their deuterated isotopologues. The column densities are derived with a constant excitation temperature of 7 K and 10 K for  $\text{HC}_3\text{N}$  and  $\text{CH}_3\text{CCH}$  and their isotopologues, respectively, and are corrected for optical depth. To derive the column density of  $\text{HC}_3\text{N}$ , we used the emission of  $\text{HCC}^{13}\text{CN}$ , assuming a constant  $^{12}\text{C}/^{13}\text{C}=68$  (Milam et al. 2005). The solid line contours indicate the  $3\sigma$  level of the integrated intensity. The dashed line contours represent 30%, 50%, and 90% of the  $\text{H}_2$  column density peak derived from *Herschel* maps (Spezzano et al. 2016). The circle in the bottom-left corner indicates the beam size of the IRAM 30 m telescope (31'). The markers in grey represent the dust peak (triangle) and the molecular emission peaks of  $\text{CH}_3\text{OH}$  (diamond),  $\text{CH}_3\text{CCH}$  (star), and  $\text{c-C}_3\text{H}_2$  (plus sign).

pared with the observations, the LTE model either overestimates the  $\text{K}=0$  line or underestimates the  $\text{K}=1$  line. Low densities in the layers traced by  $\text{CH}_3\text{CCH}$  could cause non-LTE conditions, leading to a sub-thermal excitation of the transitions and subsequently generating the emission lines different from the expected LTE profile. Figure 2 shows that the line intensity ratios also vary across the core. However, the ratio of the integrated intensity maps of the  $(5_0 - 4_0)$  over the  $(5_1 - 4_1)$  transition is roughly constant across the core, with an average value of 1.05(2). Therefore, the effect of the line variations on the derived column density of  $\text{CH}_3\text{CCH}$  and the deuteration maps should be within the error bars constrained by the derivation. The emission of  $\text{CH}_3\text{CCH}$  peaks in the north-west of L1544, away from the carbon-chain peak in the south-east. The northern part of this core is shaped by the interaction of two filaments (e.g. Spezzano et al. 2016). These structures are believed to transport fresh, chemically young gas into the north and north-west of the core (Giers et al. 2025). This replenishes the abundance of  $\text{CH}_3\text{CCH}$  and causes the molecular peak away from the carbon-chain peak in the south.

In contrast to  $\text{CH}_3\text{CCH}$ , the emission of the deuterated isotopologue  $\text{CH}_3\text{CCD}$  exhibits two strong peaks, one located in the southern part of the core at the carbon-chain peak, similar to the emission of  $\text{DC}_3\text{N}$ . The second is close to the dust peak, shifted slightly to the north-west, and coincides with the emission peak of  $\text{HDCO}$ , singly deuterated  $\text{H}_2\text{CO}$  (see Chacón-Tanarro et al. 2019). The resulting deuterium fraction map of  $\text{CH}_3\text{CCD}$  peaks close to the core centre, slightly offset towards the  $\text{CH}_3\text{OH}$  emission peak in the north-east with maximum values of 0.09(2).

A similar behaviour was also observed for the carbon chain  $\text{c-C}_3\text{H}_2$ , where the deuteration is most efficient towards the dust peak in the centre of the core (Giers et al. 2022). This, together with the similarities to  $\text{DC}_3\text{N}$  and  $\text{HDCO}$ , supports the theory that the CCH group of  $\text{CH}_3\text{CCH}$  is deuterated in the gas phase, as stated in Markwick et al. (2005).

The distribution of  $\text{CH}_2\text{DCCH}$  across L1544 mostly follows the emission of the main species. In the resulting deuteration map, however, the highest values (0.15(3)) are concentrated off-centre and towards the north-east of the core, where  $\text{CH}_3\text{OH}$  peaks (see e.g. Spezzano et al. 2016). In this region,  $\text{CH}_3\text{OH}$  traces a local density enhancement (Lin et al. 2022a), a clumpy substructure that introduces a deviation from the Bonnor-Ebert density profile used to describe the core structure in Keto et al. (2015). In fact, the  $\text{CH}_3\text{OH}$  peak seems to be the meeting point of the two larger-scale filamentary structures where L1544 is embedded. This intersection of filaments is believed to induce slow collision shocks, causing the local density enhancement (Lin et al. 2022a). The peak of the  $\text{CH}_2\text{DCCH}$  deuteration map overlaps with this higher-density region. The higher density in this area leads to a more efficient freeze-out of molecules, including  $\text{CO}$ , which drives more deuteration in the gas phase (e.g. Caselli et al. 2002b). In addition, the enhanced freeze-out onto grains leads to higher reactivity and hence drives the reactive desorption of species from dust grains (e.g. Vasyunin et al. 2017). The combination of these effects likely leads to the higher deuteration efficiency observed for  $\text{CH}_2\text{DCCH}$ .

In general,  $\text{CH}_2\text{DCCH}$  shows higher levels of deuteration (0.09-0.15) than  $\text{CH}_3\text{CCD}$  (0.07-0.09). Figure 10 compares the

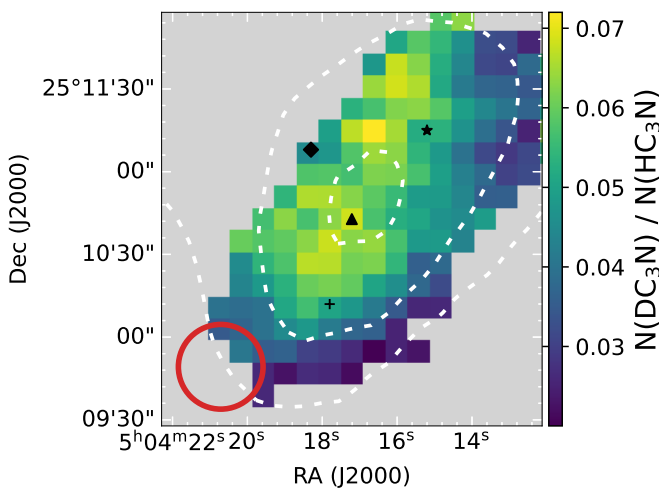


Fig. 8: Deuteration map of  $\text{HC}_3\text{N}$ . Only pixels above the  $3\sigma$  level of the respective integrated intensities are plotted. The dashed line contours represent 30%, 50%, and 90% of the  $\text{H}_2$  column density peak derived from *Herschel* maps (Spezzano et al. 2016). The circle in the bottom-left corner indicates the beam size of the IRAM 30 m telescope (31"). The markers in black represent the dust peak (triangle) and the molecular emission peaks of  $\text{CH}_3\text{OH}$  (diamond),  $\text{CH}_3\text{CCH}$  (star), and  $\text{c-C}_3\text{H}_2$  (plus sign). The corresponding D/H error map is shown in Fig. A.1.

observed deuteration values of the two isotopologues to those in other cores. Notably, the dark cloud TMC-1 shows similar behaviour to L1544: along the TMC-1 ridge,  $\text{CH}_3\text{CCD}/\text{CH}_3\text{CCH}$  shows higher values than  $\text{CH}_2\text{DCCH}/\text{CH}_3\text{CCH}$  (Markwick et al. 2005). In contrast, the protostellar cores L483 and L1551 show similar levels of deuteration in both isotopologues (Agúndez et al. 2019; Marchand et al. 2024).

A comparison between the two deuterated isotopologues (see right-hand plot in Fig. 9) shows that in L1544  $\text{CH}_2\text{DCCH}$  is 4.1–5.5 times more abundant than  $\text{CH}_3\text{CCD}$ . In contrast, Markwick et al. (2005) reported a  $\text{CH}_2\text{DCCH}/\text{CH}_3\text{CCD}$  ratio ranging between 1.2–2 along the TMC-1 ridge, which is significantly lower than the statistical value of 3. The authors attribute these lower values to decreased abundances of  $\text{H}_2\text{D}^+$  due to ambipolar diffusion, leading to a lower deuterium fractionation. On the other hand, Agúndez et al. (2019) report a ratio of  $3 \pm 1$  for  $\text{CH}_2\text{DCCH}/\text{CH}_3\text{CCD}$  in the dense core L483. The authors are able to reproduce the observed abundances of  $\text{CH}_3\text{CCH}$  and its singly and doubly deuterated isotopologues in this core with a pure gas-phase chemical model (Agúndez et al. 2021). From this, they conclude that the formation and deuteration of  $\text{CH}_3\text{CCH}$  in L483 occurs in the gas-phase rather than on grain surfaces. They propose that deuterated  $\text{CH}_3\text{CCH}$  is formed by the dissociative recombination of  $\text{C}_3\text{H}_5\text{D}^+$  and  $\text{C}_3\text{H}_6\text{D}^+$ . However, in L1544 the average  $\text{CH}_2\text{DCCH}/\text{CH}_3\text{CCD}$  ratio observed is 4.5(8), which is significantly higher than the expected statistical value of 3, showing that  $\text{CH}_2\text{DCCH}$  has a higher deuteration efficiency than  $\text{CH}_3\text{CCD}$  in this core. Therefore, additional processes must exist that enhance deuteration of the  $\text{CH}_3\text{CCH}$  methyl group, or decrease the abundance of  $\text{CH}_3\text{CCD}$ . Together with the tentative gradient of  $\text{CH}_2\text{DCCH}/\text{CH}_3\text{CCD}$  across the core, this suggests different deuteration mechanisms for the two functional groups with varying efficiency across the core.

A comparison of the emission of deuterated  $\text{CH}_3\text{CCH}$  and deuterated methanol shows interesting similarities: both

$\text{CH}_2\text{DCCH}$  and  $\text{CH}_2\text{DOH}$  peak in the northern part of L1544, close to the dust peak (see Chacón-Tanarro et al. 2019), and show significantly greater deuteration in the methyl group than in the CCH or the OH group ( $\text{CH}_2\text{DOH}/\text{CH}_3\text{OD} \geq 10$ , Bizzocchi et al. 2014). The root of this might be a common formation path for  $\text{CH}_2\text{DCCH}$  and  $\text{CH}_2\text{DOH}$  on the surfaces of dust grains, which was not considered in the pure gas-phase model used in Agúndez et al. (2021). The similarities between the  $\text{CH}_3\text{CCD}$  and  $\text{HDCO}$  emission provides another hint, as  $\text{H}_2\text{CO}$  also can be deuterated both in the gas phase and on grain surfaces. However, extensive chemical models that incorporate both gas-phase and grain-surface reactions of large hydrocarbons, are necessary to study the chemical processes and clarify the relevance of these observed trends for the isotopic fractionation of the same functional group in different molecules.

## 5. Conclusions

In this work, we studied the deuterium fraction of the carbon chains  $\text{HC}_3\text{N}$  and  $\text{CH}_3\text{CCH}$  in the pre-stellar core L1544. We analysed the emission of the species together with their singly deuterated isotopologues and  $\text{HCC}^{13}\text{CN}$ . We derived the column densities of the different species, constraining them with non-LTE radiative transfer modelling of  $\text{HC}_3\text{N}$  and  $\text{CH}_3\text{CCH}$ . The corresponding deuterium fraction maps show different behaviours in terms of distribution and level of deuteration and seem to trace different physical conditions.

$\text{HC}_3\text{N}$  shows moderate levels of deuteration, with a very extended, homogeneous distribution. This suggests that  $\text{HC}_3\text{N}$  and  $\text{DC}_3\text{N}$  trace outer layers in the envelope of the core with intermediate-density gas rather than the dense core centre, and supports a gas-phase formation of  $\text{DC}_3\text{N}$ . With non-LTE modelling, we derive a  $^{12}\text{C}/^{13}\text{C}$  ratio of  $60 \pm 20$  for  $\text{HC}_3\text{N}$  towards the dust peak of L1544, which is consistent with the value for the local ISM, 68.  $\text{CH}_2\text{DCCH}$  shows a clear deuteration peak away from the core centre, towards the north-east, coinciding with the  $\text{CH}_3\text{OH}$  molecular peak. This is likely linked to the local density enhancement in this region that enhances the CO freeze-out and therefore increases deuteration and reactive desorption.  $\text{CH}_3\text{CCD}$ , on the other hand, seems to be most efficiently formed closer to the centre of the core, where deuteration is also enhanced in other carbon chain such as  $\text{c-C}_3\text{H}_2$ .  $\text{CH}_2\text{DCCH}$  shows significantly higher levels of deuteration than  $\text{CH}_3\text{CCD}$  and is about four to five times more abundant across the core, similar to that observed for deuterated  $\text{CH}_3\text{OH}$ . This, together with the tentative trend of higher values towards the north, suggests different deuteration mechanisms for the two functional groups ( $\text{CH}_3$  and CCH) in L1544, with varying efficiency across the core.

Overall, the results of this work suggest that gas-phase reactions dominate the formation and deuteration of carbon chains in L1544, with spatial variations driven by physical structure, density, and external radiation. However, given the similarities of the deuterium fraction of  $\text{CH}_3\text{CCH}$  and  $\text{CH}_3\text{OH}$ , an additional deuteration pathway of  $\text{CH}_3\text{CCH}$  might exist on the surfaces of dust grains. This shows the importance of understanding the ongoing chemical processes when using deuterated molecules as tools to study the interface between the dense core and the surrounding cloud.

*Acknowledgements.* We wish to thank the anonymous referee for their constructive comments. The authors wish to thank the Max Planck Society for financial support.

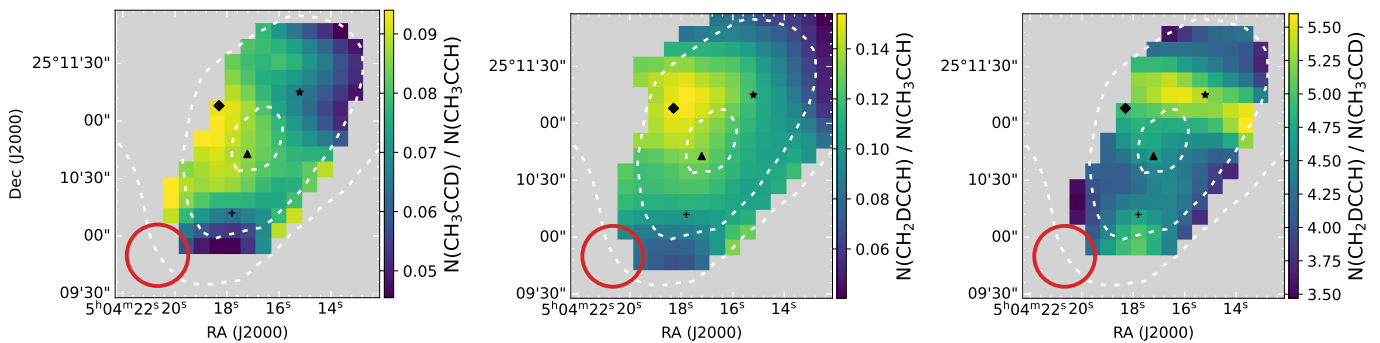


Fig. 9: Deuteration maps of  $\text{CH}_3\text{CCH}$ . Only pixels above the  $3\sigma$  level of the respective integrated intensities are plotted. The dashed line contours represent 30%, 50%, and 90% of the  $\text{H}_2$  column density peak derived from *Herschel* maps (Spezzano et al. 2016). The circle in the bottom-left corner indicates the beam size of the IRAM 30 m telescope (31"). The markers in black represent the dust peak (triangle) and the molecular emission peaks of  $\text{CH}_3\text{OH}$  (diamond),  $\text{CH}_3\text{CCH}$  (star), and  $\text{c-C}_3\text{H}_2$  (plus sign). The corresponding D/H error maps are shown in Fig. A.1.

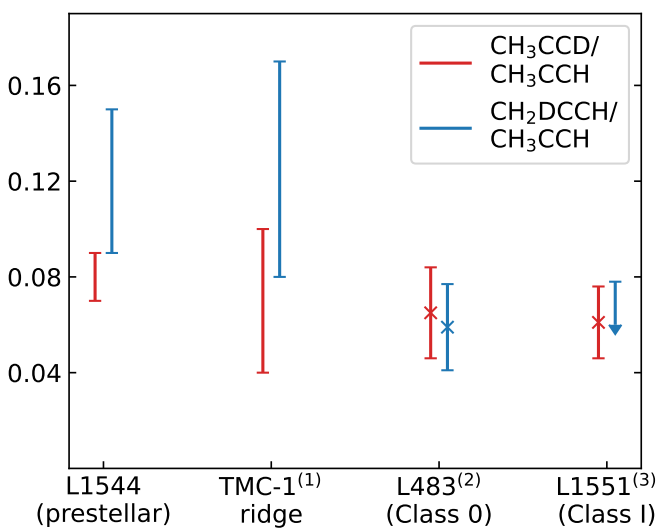


Fig. 10: Comparison of the deuteration of  $\text{CH}_3\text{CCH}$  towards different cores. For L1544 and TMC-1, the given range covers minimum to maximum values across the cores, while for L483 and L1551 single values are given including error bars or upper limits. References include: (1) Markwick et al. (2005), (2) Agúndez et al. (2019), (3) Marchand et al. (2024).

## References

Agúndez, M., Marcelino, N., Cernicharo, J., Roueff, E., & Tafalla, M. 2019, *A&A*, 625, A147

Agúndez, M., Roueff, E., Cabezas, C., Cernicharo, J., & Marcelino, N. 2021, *A&A*, 649, A171

Bauer, A. & Burie, J. 1969, *C. R. Acad. Sci. Paris, B* 268, 800

Ben Khalifa, M., Dárra, B., & Loreau, J. 2024, *A&A*, 683, A53

Bianchi, E., Remijan, A., Codella, C., et al. 2023, *ApJ*, 944, 208

Bizzocchi, L., Caselli, P., Spezzano, S., & Leonardo, E. 2014, *A&A*, 569, A27

Bonnor, W. B. 1956, *MNRAS*, 116, 351

Buhl, D. & Snyder, L. E. 1973, in *Molecules in the Galactic Environment*, ed. M. A. Gordon & L. E. Snyder, 187

Calcutt, H., Willis, E. R., Jørgensen, J. K., et al. 2019, *A&A*, 631, A137

Caselli, P., Pineda, J. E., Sipilä, O., et al. 2022, *ApJ*, 929, 13

Caselli, P., Walmsley, C. M., Tafalla, M., Dore, L., & Myers, P. C. 1999, *ApJ*, 523, L165

Caselli, P., Walmsley, C. M., Zucconi, A., et al. 2002a, *ApJ*, 565, 331

Caselli, P., Walmsley, C. M., Zucconi, A., et al. 2002b, *ApJ*, 565, 344

Chacón-Tanarro, A., Caselli, P., Bizzocchi, L., et al. 2019, *A&A*, 622, A141

Chantzos, J., Spezzano, S., Caselli, P., et al. 2018, *ApJ*, 863, 126

Chapillon, E., Dutrey, A., Guilloteau, S., et al. 2012, *ApJ*, 756, 58

Crapsi, A., Caselli, P., Walmsley, C. M., et al. 2005, *ApJ*, 619, 379

Creswell, R. A., Winnewisser, G., & Gerry, M. C. L. 1977, *Journal of Molecular Spectroscopy*, 65, 420

Dalgarno, A. & Lepp, S. 1984, *ApJ*, 287, L47

Ebert, R. 1955, *ZAp*, 37, 217

Faure, A., Lique, F., & Wiesenfeld, L. 2016, *MNRAS*, 460, 2103

Fontani, F., Cesaroni, R., Caselli, P., & Olmi, L. 2002, *A&A*, 389, 603

Fukuzawa, K. & Osamura, Y. 1997, *ApJ*, 489, 113

Fuller, G. A. & Myers, P. C. 1992, *ApJ*, 384, 523

Gerin, M., Combes, F., Wlodarczak, G., Encrénaz, P., & Laurent, C. 1992, *A&A*, 253, L29

Giers, K., Spezzano, S., Alves, F., et al. 2022, *A&A*, 664, A119

Giers, K., Spezzano, S., Caselli, P., et al. 2023, *A&A*, 676, A78

Giers, K., Spezzano, S., Lin, Y., et al. 2025, *A&A*, 699, A103

Ginsburg, A., Koch, E., Robitaille, T., et al. 2019, *radio-astro-tools/spectral-cube*: v0.4.4

Goldsmith, P. F. & Langer, W. D. 1999, *ApJ*, 517, 209

Gratier, P., Majumdar, L., Ohishi, M., et al. 2016, *ApJS*, 225, 25

Guzmán, A. E., Guzmán, V. V., Garay, G., Bronfman, L., & Hechenleitner, F. 2018, *ApJS*, 236, 45

Hickson, K. M., Wakelam, V., & Loison, J.-C. 2016, *Molecular Astrophysics*, 3, 1

Hily-Blant, P., Faure, A., Vastel, C., et al. 2018, *MNRAS*, 480, 1174

Howe, D. A., Millar, T. J., Schilke, P., & Walmsley, C. M. 1994, *MNRAS*, 267, 59

Iraqi, M., Petrank, A., Peres, M., & Lifshitz, C. 1990, *International Journal of Mass Spectrometry and Ion Processes*, 100, 679

Juvela, M. 2020, *A&A*, 644, A151

Keto, E., Caselli, P., & Rawlings, J. 2015, *MNRAS*, 446, 3731

Langer, W. D., Schloerb, F. P., Snell, R. L., & Young, J. S. 1980, *ApJ*, 239, L125

Leguenne, M., Demaison, J., Wlodarczak, G., & Marsden, C. 1993, *Journal of Molecular Spectroscopy*, 160, 471

Lin, Y., Spezzano, S., Sipilä, O., Vasyunin, A., & Caselli, P. 2022a, *A&A*, 665, A131

Lin, Y., Wyrowski, F., Liu, H. B., et al. 2022b, *A&A*, 658, A128

Mallinson, P. D. & de Zafra, R. L. 1978, *Molecular Physics*, 36, 827

Mangum, J. G. & Shirley, Y. L. 2015, *PASP*, 127, 266

Marchand, P., Coutens, A., Scigliuto, J., et al. 2024, *A&A*, 687, A195

Markwick, A. J., Charnley, S. B., Butner, H. M., & Millar, T. J. 2005, *ApJ*, 627, L117

Milam, S. N., Savage, C., Brewster, M. A., Ziurys, L. M., & Wyckoff, S. 2005, *ApJ*, 634, 1126

Morris, M., Turner, B. E., Palmer, P., & Zuckerman, B. 1976, *ApJ*, 205, 82

Müller, H. S. P., Thorwirth, S., Roth, D. A., & Winnewisser, G. 2001, *A&A*, 370, L49

Öberg, K. I., Boamah, M. D., Fayolle, E. C., et al. 2013, *ApJ*, 771, 95

Pagani, L., Salez, M., & Wannier, P. G. 1992, *A&A*, 258, 479

Parker, D. S. N. & Kaiser, R. I. 2017, *Chem. Soc. Rev.*, 46, 452

Pety, J. 2005, in *SF2A-2005: Semaine de l’Astrophysique Française*, ed. F. Caselli, T. Contini, J. M. Hameury, & L. Pagani, 721

Redaelli, E., Bizzocchi, L., Caselli, P., et al. 2019, *A&A*, 629, A15

Rivilla, V. M., Colzi, L., Fontani, F., et al. 2020, *MNRAS*, 496, 1990

Sakai, N., Sakai, T., Hirota, T., & Yamamoto, S. 2009, *ApJ*, 702, 1025

Schiff, H. I. & Bohme, D. K. 1979, *ApJ*, 232, 740

Schöier, F. L., van der Tak, F. F. S., van Dishoeck, E. F., & Black, J. H. 2005, *A&A*, 432, 369

Shingledecker, C. N., Lee, K. L. K., Wandishin, J. T., et al. 2021, *A&A*, 652, L12

Sims, I. R., Queffelec, J.-L., Travers, D., et al. 1993, *Chemical Physics Letters*, 211, 461

Sipilä, O., Caselli, P., Redaelli, E., Juvela, M., & Bizzocchi, L. 2019, *MNRAS*, 487, 1269

Spezzano, S., Bizzocchi, L., Caselli, P., Harju, J., & Brünken, S. 2016, *A&A*, 592, L11

Spezzano, S., Brunken, S., Schilke, P., et al. 2013, in 68th International Symposium on Molecular Spectroscopy, ETI08

Spezzano, S., Caselli, P., Bizzocchi, L., Giuliano, B. M., & Lattanzi, V. 2017, *A&A*, 606, A82

Spezzano, S., Caselli, P., Sipilä, O., & Bizzocchi, L. 2022, *A&A*, 664, L2

Turner, B. E. 1971, *ApJ*, 163, L35

Turner, B. E. 2001, *ApJS*, 136, 579

Turner, B. E., Terzieva, R., & Herbst, E. 1999, *ApJ*, 518, 699

van Dishoeck, E. F., Blake, G. A., Jansen, D. J., & Groesbeck, T. D. 1995, *ApJ*, 447, 760

Vastel, C., Ceccarelli, C., Lefloch, B., & Bachiller, R. 2014, *ApJ*, 795, L2

Vasyunin, A. I., Caselli, P., Dulieu, F., & Jiménez-Serra, I. 2017, *ApJ*, 842, 33

Walmsley, C. M., Flower, D. R., & Pineau des Forets, G. 2004, *A&A*, 418, 1035

Walmsley, C. M., Winnewisser, G., & Toelle, F. 1980, *A&A*, 81, 245

Ward-Thompson, D., Motte, F., & Andre, P. 1999, *MNRAS*, 305, 143

Wes McKinney. 2010, in Proceedings of the 9th Python in Science Conference, ed. Stéfan van der Walt & Jarrod Millman, 56 – 61

## Appendix A: Additional material on deuteration maps

### Appendix A.1: Uncertainties of deuteration maps

Figure A.1 shows the uncertainties on the deuteration maps of  $\text{HC}_3\text{N}$  and  $\text{CH}_3\text{CCH}$  presented in Figs. 8 and 9, respectively.

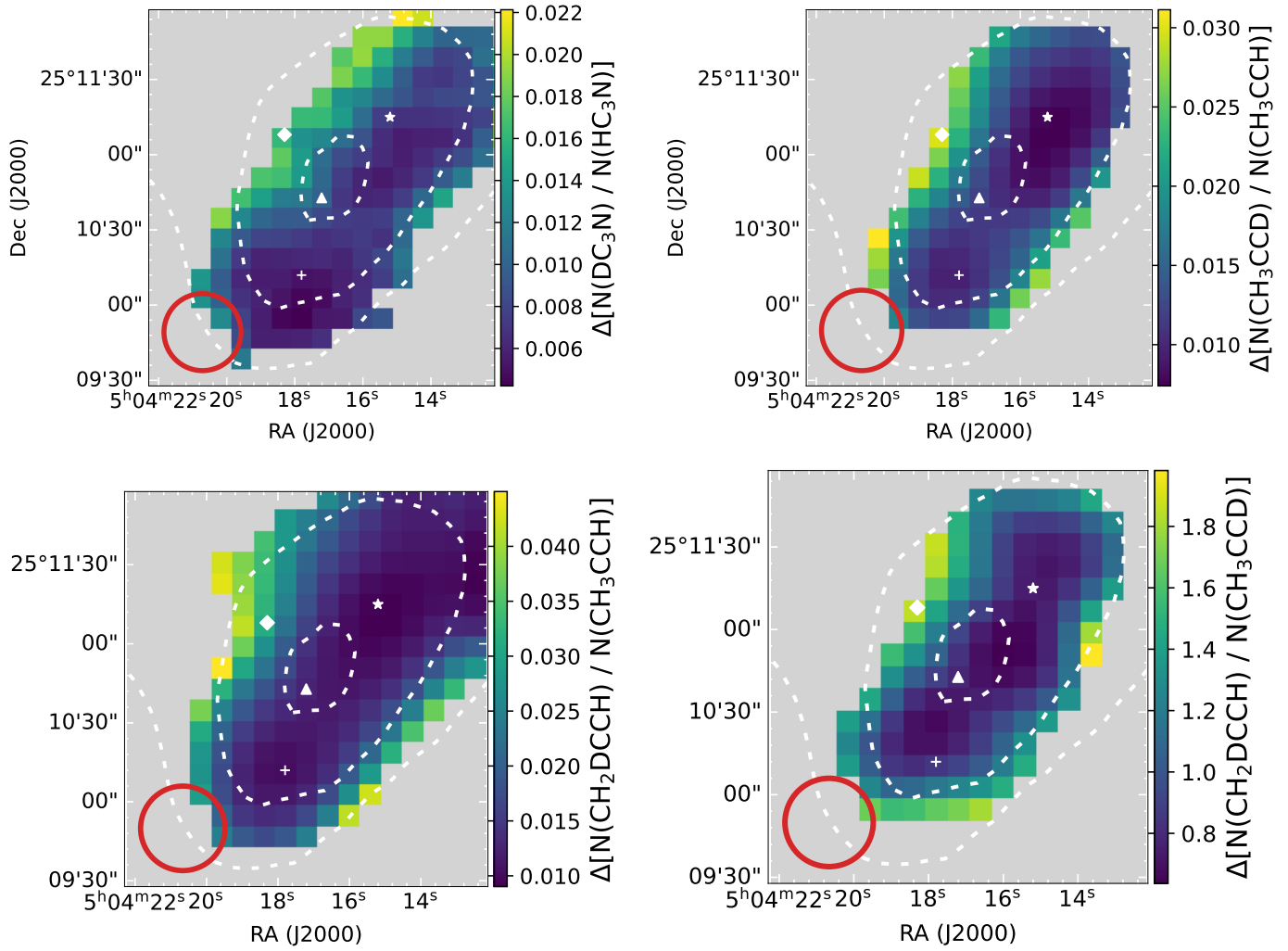


Fig. A.1: Error maps of the deuteration maps for  $\text{HC}_3\text{N}$  and  $\text{CH}_3\text{CCH}$  (presented in Figs. 8 and 9, respectively). Only pixels above the  $3\sigma$  level of the respective integrated intensities are plotted. The dashed line contours represent 30%, 50%, and 90% of the  $\text{H}_2$  column density peak derived from *Herschel* maps (Spezzano et al. 2016). The circle in the bottom-left corner indicates the beam size of the IRAM 30 m telescope (31''). The markers in white represent the dust peak (triangle) and the molecular emission peaks of  $\text{CH}_3\text{OH}$  (diamond),  $\text{CH}_3\text{CCH}$  (star), and  $\text{c-C}_3\text{H}_2$  (plus sign).

### Appendix A.2: Deuteration of $\text{CH}_3\text{CCH}$ derived from $K=1$

Figure A.2 shows the column density map of  $\text{CH}_3\text{CCH}$  derived from the  $(5_1 - 4_1)$  transition and the resulting deuteration maps. The distribution of the emission of the  $K=1$  transition is identical to the  $K=0$  transition, resulting in an identical morphology the deuterium fraction. However, the peak column density derived from  $K=1$  with an excitation temperature of 10 K is a factor of 2 higher compared to the values derived from  $K=0$ . This results in substantially lower deuteration levels, with peak values of 0.045(5) and 0.07(1) for  $\text{N}(\text{CH}_3\text{CCD})/\text{N}(\text{CH}_3\text{CCH})$  and  $\text{N}(\text{CH}_2\text{DCCH})/\text{N}(\text{CH}_3\text{CCH})$ , respectively. However, the relation between the two deuterated isotopologues does not change, and therefore, the conclusions drawn from them are not affected.

## Appendix B: Spectra at molecular peaks

Figure B.1 presents spectra of the observed transitions, extracted towards the three molecular emission peaks ( $\text{CH}_3\text{OH}$ ,  $\text{CH}_3\text{CCH}$ ,  $\text{c-C}_3\text{H}_2$ ) and the dust peak of L1544, by using a circular aperture with a diameter corresponding to the telescope beam size (31'').  $\text{CH}_3\text{CCH}$  and  $\text{CH}_2\text{DCCH}$  are only represented with one transition each, as they are discussed separately in Sect. 3 and Fig. 2.

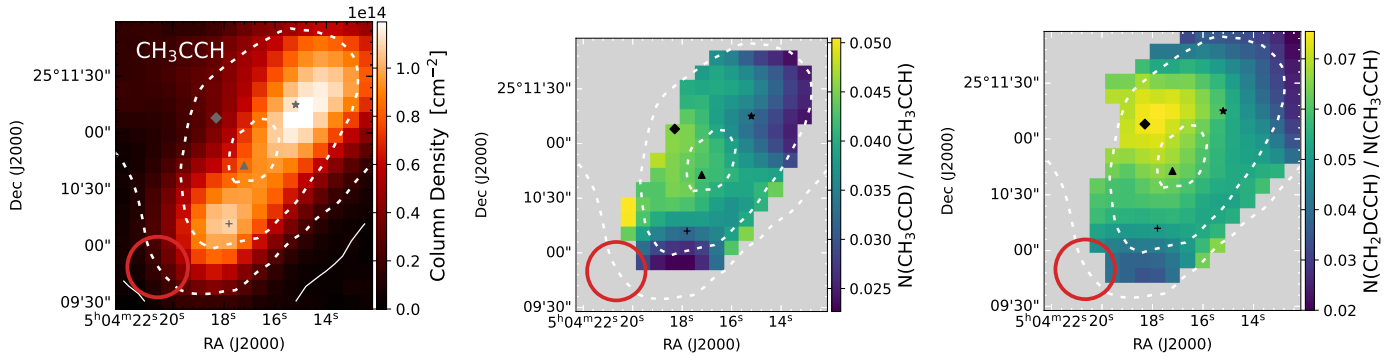


Fig. A.2: *Left:* Column density map of  $\text{CH}_3\text{CCH}$  derived with the  $(5_1 - 4_1)$  transition. The solid contour indicates the  $3\sigma$  level of the column density. The markers represent the dust peak (triangle) and the molecular emission peaks of  $\text{CH}_3\text{OH}$  (diamond),  $\text{CH}_3\text{CCH}$  (star), and  $\text{c-C}_3\text{H}_2$  (plus sign). *Right:* Corresponding deuteration maps. Only pixels above the  $3\sigma$  level of the respective integrated intensities are plotted.

The extraction locations of the spectra are marked in Fig. 1. The corresponding linewidths and velocities of the spectra at the four extraction locations are derived with Gaussian fitting and given in Table B.1.

The spectra show that the brightest emission of all observed molecules is detected towards the  $\text{c-C}_3\text{H}_2$  peak located in the south of the core. In this region, the core is less protected from the ISRF, which drives photochemistry and leads to an active carbon chemistry and an increased abundance of C-bearing species. As all observed molecules in this study are essentially carbon chains, they are most efficiently formed in such conditions. However, the linewidths observed towards the  $\text{CH}_3\text{CCH}$  peak (and the dust peak) are significantly larger than towards the  $\text{c-C}_3\text{H}_2$  peak. This indicates the location where the flow of material from the outer regions of the core (in the direction of the main filament) reaches the dense core and undergoes a local slow shock (as in the case of  $\text{CH}_3\text{OH}$  at the  $\text{CH}_3\text{OH}$  peak, see Lin et al. 2022a), causing broader linewidths. The spectra of  $\text{DC}_3\text{N}$  seem to show rather flat line profiles towards the  $\text{CH}_3\text{CCH}$  peak. As  $\text{DC}_3\text{N}$  is tracing less dense gas in the outer envelope of the core, the broader linewidth is likely caused by the larger turbulence present in those outer parts (e.g. Fuller & Myers 1992).

Table B.1: Comparison of the linewidths and velocities of the observed transitions at different locations in L1544 (dust peak,  $\text{CH}_3\text{OH}$  peak,  $\text{CH}_3\text{CCH}$  peak, and  $\text{c-C}_3\text{H}_2$  peak, see Fig. 1).

Molecule	Transition	Dust peak		$\text{CH}_3\text{OH}$ peak		$\text{CH}_3\text{CCH}$ peak		$\text{c-C}_3\text{H}_2$ peak	
		$V_{\text{LSR}}$	FWHM	$V_{\text{LSR}}$	FWHM	$V_{\text{LSR}}$	FWHM	$V_{\text{LSR}}$	FWHM
$\text{HC}_3\text{N}$	11 – 10	7.250(7)	0.197(7)	7.239(5)	0.180(5)	7.200(6)	0.204(6)	7.268(3)	0.152(3)
$\text{HCC}^{13}\text{CN}$	10 – 9	7.19(2)	0.21(2)	7.17(4)	0.19(4)	7.13(2)	0.24(2)	7.239(6)	0.141(6)
$\text{DC}_3\text{N}$	10 – 9	7.22(1)	0.19(1)	7.18(2)	0.18(2)	7.141(9)	0.203(9)	7.285(4)	0.130(3)
$\text{CH}_3\text{CCH}$	$5_0 - 4_0$	7.24(3)	0.19(3)	7.19(2)	0.18(2)	7.17(3)	0.20(3)	7.26(2)	0.13(2)
$\text{CH}_3\text{CCD}$	$6_0 - 5_0$	7.17(4)	0.25(4)	7.18(5)	0.21(5)	7.07(3)	0.20(3)	7.26(2)	0.12(1)
$\text{CH}_2\text{DCCH}$	$6_{06} - 5_{05}$	7.151(9)	0.195(9)	7.10(2)	0.18(2)	7.062(8)	0.193(8)	7.229(6)	0.136(5)

**Notes.** The parameters are derived from the spectra presented in Fig. B.1 using Gaussian fitting, and given in units of  $\text{km s}^{-1}$ .

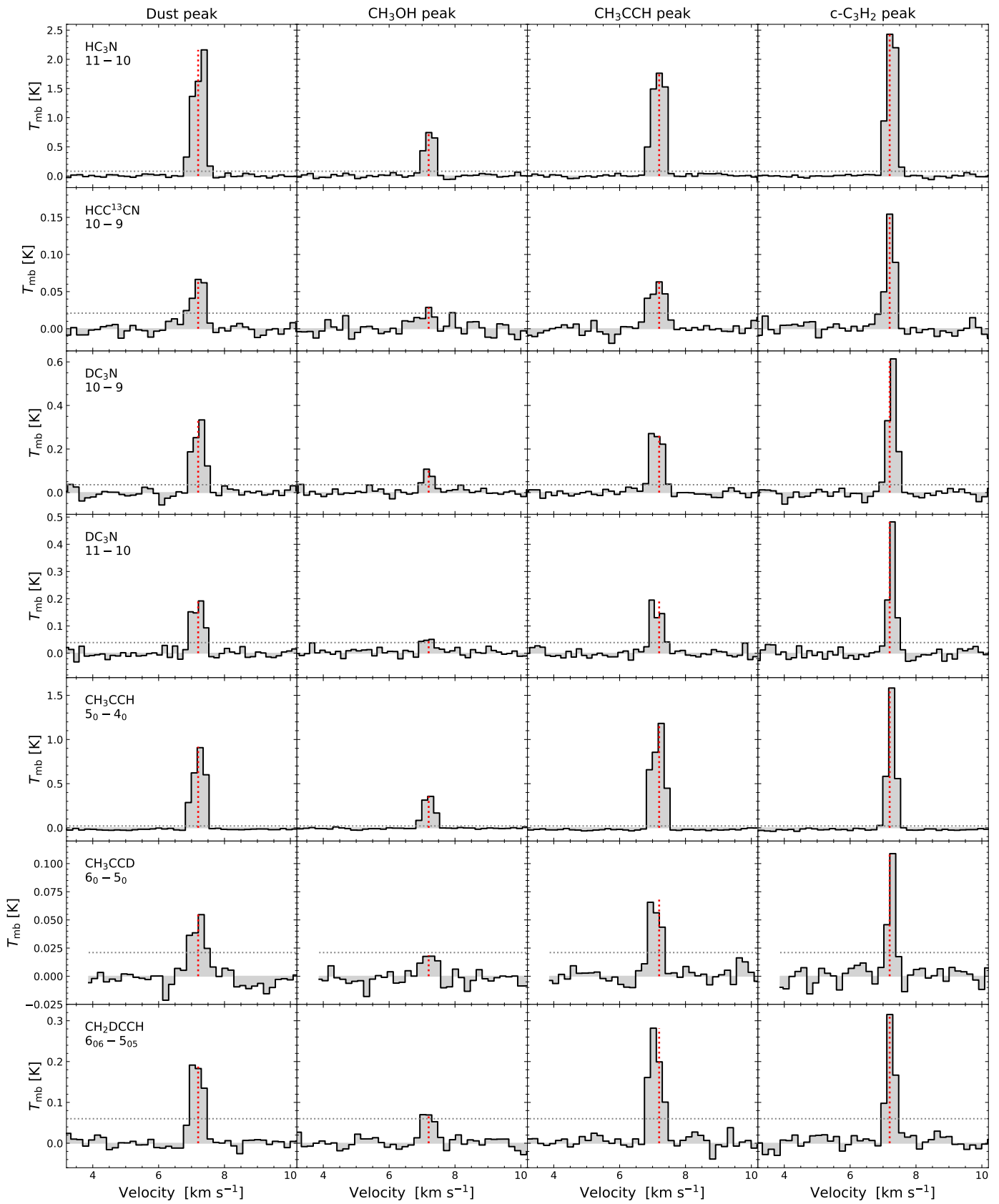


Fig. B.1: Spectra of the observed transitions, extracted at the dust peak, the  $\text{CH}_3\text{OH}$  peak, the  $\text{CH}_3\text{CCH}$  peak, and the  $\text{c-C}_3\text{H}_2$  peak of L1544. The extraction locations of the spectra, as well as the telescope beam used as aperture, are indicated in Fig. 1. The horizontal line indicates the  $3\sigma$  confidence level, and the vertical line indicates the systemic velocity of the source.